DISEASES AND DISORDERS

C-mannosyltransferase DPY19L1L-mediated Reissner Fiber formation is critical for zebrafish (*Danio rerio*) body axis straightening

Guiyou Tian[1]†, Lirong Huang[1]†, Zhaopeng Xu[1]†, Chen Lu[1], Wei Yuan[1], Yulin Wu[1], Zhipeng Liao[1], Jia Gao[1], Qiang Luo[1], Bo Cheng[1], Xinjun Liao[2], Huiqiang Lu[3]*

The successful secretion and assembly of subcommissural organ (SCO)–spondin are crucial for Reissner Fiber (RF) formation and body axis straightening in zebrafish. However, the mechanisms underlying RF formation remain largely unknown. Here, we report that the C-mannosyltransferase *dpy19l1l* (dumpy-19 like 1 like) is expressed in the spinal cord during zebrafish embryonic development. Mutation in *dpy19l1l* resulted in idiopathic scoliosis (IS)–like body axis curvature in the absence of muscle or cilia defects. URP2 expression was down-regulated in *dpy19l1l*$^{-/-}$ mutants. Notably, RF formation was impaired in *dpy19l1l*$^{-/-}$ mutants, and a similar phenotype was induced in wild-type embryos by injecting messenger RNA encoding a C-mannosylation catalytic site-mutated *dpy19l1l* variant (E106A *mdpy19l1l*). Furthermore, E106A mDPY19L1L failed to glycosylate Flag-tagged SCO-spondin TSRs (thrombospondin type 1 repeats). Our findings suggest that DPY19L1L-mediated C-mannosylation of SCO-spondin TSRs promotes RF formation and URP2 induction, representing a critical supplementary mechanism for body axis straightening in zebrafish.

INTRODUCTION

Zebrafish (*Danio rerio*) has emerged as a powerful model organism for investigating idiopathic scoliosis (IS) pathogenesis, particularly because the protein tyrosine kinase 7 (*ptk7*) mutant zebrafish has been defined as a model of IS (*1*–*5*). Studies in zebrafish have established that cilia-driven cerebrospinal fluid (CSF) flow coordinates body axis straightening through a conserved morphogenetic mechanism. This process requires continuous secretion of SCO-spondin by the subcommissural organ (SCO) and its assembly into Reissner Fiber (RF) (*6*–*14*). In the spinal cord, RF serves as a transport conduit for monoamines and signaling molecules. These monoamines induce neuronal production of neuropeptides (*11*, *15*–*22*), which subsequently activate receptors to mediate body axis straightening. Urotensin-related peptides (URPs), secreted by CSF-contacting neurons (CSF-cNs), function as downstream effectors in this pathway. Through receptor activation, URPs trigger paravertebral slow-twitch muscle contraction and maintain body straightness (*5*, *15*, *16*). Although RF integrity is required for maintaining zebrafish body axis morphology, the molecular machinery governing its biogenesis remains poorly elucidated.

Protein C-mannosylation was initially identified in human RNase2 (*23*), with tryptophan C-mannosylation representing the sole characterized form of protein C-linked glycosylation (*24*). This modification enhances expression, secretion and additional adhesion of thrombospondin type 1 repeats (TSRs)–containing proteins (*25*–*27*). TSRs are small motifs found in diverse cell surface receptors and secreted proteins, and over 60 distinct human proteins contain TSRs (*26*, *28*). Most TSR domains contain two or three conserved tryptophan residues within their N-terminal regions, with the WxxWxxWxxC sequence constituting a hallmark structural signature (*26*, *29*–*31*).

DPY-19 constitutes an evolutionarily conserved family of multipass transmembrane proteins, with four mammalian homologs (DPY-19L1-L4) identified to date (*26*, *32*, *33*). Biochemical studies revealed DPY19L1 and DPY19L3 as principal mediators of TSR C-mannosylation: DPY19L1 predominantly catalyzes C-mannosylation at the first two tryptophan residues, whereas DPY19L3 modifies the third position within TSR domains (*26*). To date, the investigation of DPY19L1-L4 is still very limited and their biological functions remain largely unknown. In *Caenorhabditis elegans*, DPY-19 mediates C-mannosylation of MIG-21 (abnormal cell MIGration-21) and UNC-5 (UNCoordinated-5), with this posttranslational modification being critical for maintaining their solubility and secretion ability (*34*). Mammalian cell studies demonstrated that DPY19L1-dependent C-mannosylation is essential for endoplasmic reticulum (ER)–to–plasma membrane trafficking of the netrin receptor UNC5A (UNCoordinated-5 A) (*26*). Mouse studies further revealed DPY19L1's neurodevelopmental roles in orchestrating neuronal migration and modulating neurite extension during cortical development (*32*, *35*).

Both *dpy19l1l* and *dpy19l3* have been identified in zebrafish. Mutation in *dpy19l1l* present human IS-like spinal curvature phenotypes (http://zfin.org/search?category=&q=dpy19), manifesting as pronounced body axis curvature. This aligns with clinical evidence showing that lower methylation variability near the *dpy19l1* locus correlates with IS severity progression (*36*). However, the mechanisms of body axis curvature induced by *dpy19l1l* defect have not been studied in detail. Although biochemical functions of DPY-19 and its homologs are becoming increasingly understood, their modification substrates and physiological roles in development and disease remain obscure. Through comprehensive analysis of the phenotype and biological features of *dpy19l1l* knockout zebrafish, we found that DPY19L1L promotes RF formation through C-mannosylation of SCO-spondin TSRs. This C-mannosylation–dependent process is essential for zebrafish body axis morphogenesis. Our findings disclose

[1]Jiangxi Provincial Key Laboratory of Synthetic Pharmaceutical Chemistry, School of Geography and Environmental Engineering, Gannan Normal University, Ganzhou 341000, China. [2]Affiliated Hospital of Jinggangshan University, College of Life Sciences, Jinggangshan University, Ji'an 343000, Jiangxi, China. [3]Center for Clinical Medicine Research, First Affiliated Hospital of Gannan Medical University, Ganzhou 341000, Jiangxi Province, China.
*Corresponding author. Email: luhq2@126.com
†These authors contributed equally to this work.

a hidden role of DPY19L1L in zebrafish body axis, maintaining and provide previously unidentified mechanistic insights into the pathogenesis of IS.

RESULTS

Mutation of d*py19l1l* causes IS-like body axis curvature in zebrafish

Phenotypic data from the ZFIN database demonstrate that *dpy19l1l* disruption induces body axis curvature, consistent with clinical findings showing reduced *dpy19l1* methylation variability in patients with IS compared to controls (*36*). Given the clinical hallmark of IS onset during prepubescence (*1*, *2*, *36*), we investigated *dpy19l1l* expression patterns during early zebrafish development. Through whole-mount in situ hybridization (WMISH) using *dpy19l1l*-specific riboprobes, we detected transcriptional signals adjacent to the presumptive spinal cord region at early developmental stages (Fig. 1A). Subsequent fluorescence in situ hybridization (FISH) at 36 hours postfertilization (hpf) precisely localized *dpy19l1l* expression to both spinal cord tissues and floor plate regions (Fig. 1B). These data suggest that *dpy19l1l* probably plays some specific functions in zebrafish spinal cord, particularly in the early stages of development. To approach this hypothesis, we applied a microinjection of morpholino (MO) antisense oligonucleotide targeting *dpy19l1l*. We found that knocking down *dpy19l1l* in zebrafish displayed severe body axis curvature (Fig. 1, C and D). We further generated *dpy19l1l*$^{+/-}$ heterozygous mutants via CRISPR-Cas9 (fig. S1) and approximately a quarter of *dpy19l1l*$^{+/-}$ intercrossed progeny (n = 22/87; fig. S2) developed spinal curvatures at juvenile stages (Fig. 1E). In addition, mutants exhibited severe motor impairment, with substantial reduced swimming distances (fig. S3, A and B). Furthermore, the mutant larvae eventually die around 12 days postfertilization (fig. S3C), probably due to difficulty eating. Prior studies demonstrated that releasing *SCO-spondin* mutant embryos from the chorion at 24 hpf ameliorates ventral axial curvature, enabling their development into adults with IS-like phenotypes (*16*). To verify whether this physiological characteristic exists in *dpy19l1l*$^{-/-}$ zebrafish, we removed the chorion of *dpy19l1l*$^{+/-}$ zebrafish intercrossed embryos at 24 hpf and maintained the larvae under normal conditions. Some of the larvae developed with less severely curved body axis and subsequently matured into adults (Fig. 1F). We also recorded the survival rate of chorion released *dpy19l1l*$^{-/-}$ and sibling control zebrafish. The result indicated that the long-term survival rate of chorion released *dpy19l1l*$^{-/-}$ mutants was lower than that of sibling control (fig. S3D). Then, the vertebral columns of the adults were analyzed by alizarin red S (ARS) staining (Fig. 1G), and our result indicated that the spine morphology in *dpy19l1l*$^{-/-}$ adult zebrafish is highly similar to that described in other IS-like spinal curvature mutants zebrafish (*11*, *14*–*16*). Together, these data strongly support the crucial role for *dpy19l1l* in development and body axis straightening during larval stages of the zebrafish, and mutation of *dpy19l1l* could lead to IS-like spinal curvature.

Urp2 expression is down-regulated in *dpy19l1l* mutants

To investigate whether axial curvature in *dpy19l1l*$^{-/-}$ mutants stems from myogenic defects, we analyzed larval muscle structure through immunohistochemistry. Immunostaining with muscle-specific antibodies against F59, Prox1a, and Engrailed revealed no structural differences between mutants and control siblings (fig. S4). These results rule out myogenic defects as the cause of the observed axial curvature. Ciliary integrity is required for normal CSF flow, a process critical for zebrafish axial straightening (*6*–*14*). To assess whether *dpy19l1l*$^{-/-}$ axial curvature arises from ciliary defects or impaired CSF dynamics, we (i) immunostained cilia using acetylated tubulin antibody and (ii) tracked CSF flow via fluorescent dye injection into brain ventricles (*15*). We found that both cilia morphology and CSF flow patterns showed no abnormalities in *dpy19l1l* mutants (fig. S5). These results exclude cilia-driven CSF defects as the causative mechanism of axial curvature of *dpy19l1l*$^{-/-}$ mutants.

Given the well-documented role of the RF and its constituent protein SCO-spondin in zebrafish body axis straightening (*6*, *7*, *9*, *12*, *13*), we investigated potential differences in SCO-spondin expression between control siblings and *dpy19l1l*$^{-/-}$ zebrafish. Quantitative polymerase chain reaction (qPCR) analysis combined with in situ hybridization revealed no significant difference in *SCO-spondin* transcript levels between control and *dpy19l1l*$^{-/-}$ mutants (fig. S6). The function of adrenergic activation in rescuing body axis curvature defects caused by RF impairment has been well established (*8*, *15*). To investigate whether adrenergic activation could similarly ameliorate the curvature phenotype in *dpy19l1l*$^{-/-}$ mutants as previously reported (*15*), we administered epinephrine treatment. Following this intervention, we observed significant restoration of body axis morphology in *dpy19l1l*$^{-/-}$ mutants (Fig. 2, A and B), despite concurrent development of severe pericardial edema (Fig. 2A). To investigate whether adrenergic signaling-associated downstream genes in the spinal cord were altered in *dpy19l1l*$^{-/-}$ mutants, we performed quantitative reverse transcription polymerase chain reaction (qRT-PCR) analyses of *urp1*, *urp2*, and their cognate receptor *uts2ra*. Like in *SCO-spondin* mutants (*8*), *urp2* expression was substantial down-regulated in *dpy19l1l* mutants, whereas *urp1* levels showed a modest reduction (Fig. 2C). To validate the tissue-specific expression patterns of *urp* genes in *dpy19l1l*$^{-/-}$ mutants and wild-type siblings, we conducted in situ hybridization experiments. Consistent with the qRT-PCR results, in situ hybridization confirmed near-complete loss of *urp2* expression in mutants (Fig. 2D). These findings collectively indicate defective adrenergic signaling and URP2 in *dpy19l1l*$^{-/-}$ mutants.

URP2 administration rescues spinal curvature in *dpy19l1l*$^{-/-}$ mutants

The observed *urp2* down-regulation prompted us to investigate whether URP2 peptide supplementation could ameliorate body axis defects in *dpy19l1l*$^{-/-}$ mutants. Therefore, we intracerebroventricularly (Fig. 3A) injected synthetic URP2 into both wild-type siblings and *dpy19l1l*$^{-/-}$ mutants. Mutant larvae exhibited pronounced phenotypic rescue, with significant alleviation of spinal curvature (Fig. 3, B to F). The survival of URP2-injected zebrafish was calculated at 10 days postfertilization (dpf), and the results showed that the average survival rate of control and mutant without URP2 injection at 10 dpf was 90.03 and 63.14%, whereas the URP2-injected control and mutants was 65.10 and 49.85%, respectively. This result indicated that URP2 injection had a slight influence on the 10-day survival rate in zebrafish (Fig. 3G). Despite this, URP2-treated mutants demonstrated locomotor capacity comparable to wild-type controls at 10 dpf, whereas untreated mutants showed near-complete loss of swimming ability (Fig. 3, H and I). These findings provide strong evidences that *dpy19l1l*$^{-/-}$ mutant zebrafish has a deficiency in URP2.

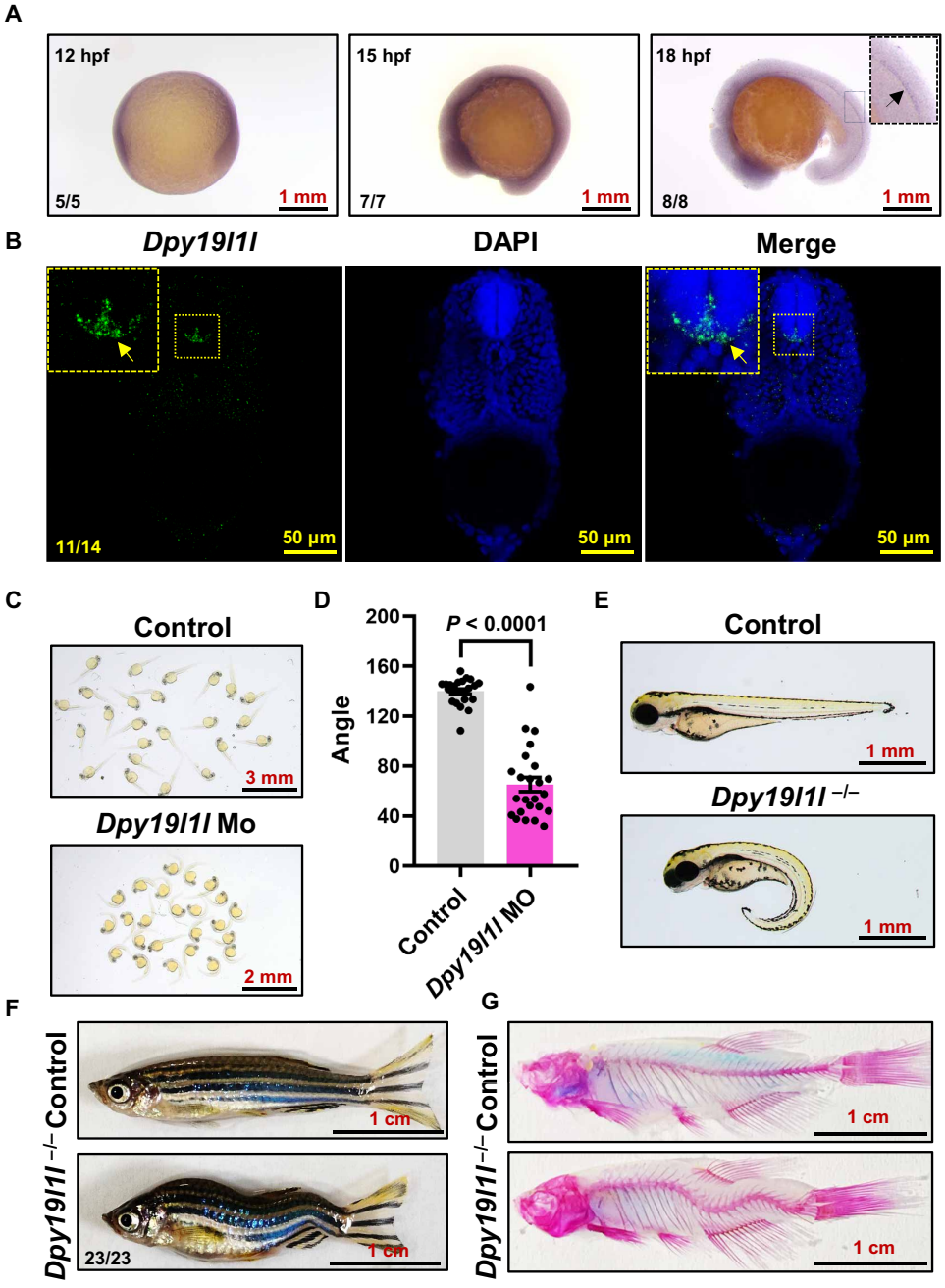

Fig. 1. *Dpy19l1l* expression in the spinal cord and its mutation leading to IS-like body axis curvature. (**A**) WMISH of *dpy19l1l* at 12 to 18 hpf. The arrow in the enlarged view of 18 hpf larvae indicates dpy19l1l expression. (**B**) Confocal projection of longitudinal trunk sections from 36 hpf larvae hybridized with a fluorescence riboprobe and 4′,6-diamidino-2-phenylindole (DAPI). The yellow arrow in the enlarged view marks *dpy19l1l* expression in spinal cord floor plate cells. (**C**) Phenotypes of *dpy19l1l* MO-injected larvae at 36 hpf, showing body axis curvature. (**D**) Quantification of body axis angles using ImageJ (bar graph; means ± SEM, $n = 24$). The *P* value (unpaired *t* test) is indicated above bars. (**E**) External phenotypes of control sibling and *dpy19l1l*$^{-/-}$ mutants at 2 dpf. (**F**) External phenotypes of adult control sibling and *dpy19l1l*$^{-/-}$ mutants. (**G**) ARS staining of adult control sibling and *dpy19l1l*$^{-/-}$ mutants.

Dpy19l1l-deficient zebrafish lack RF

The role of RF in regulating *urp* gene expression and maintaining axial morphology in zebrafish is well documented (*8*, *16*, *37*). RF is a thread suspended in CSF and largely composed of the giant glycoprotein SCO-spondin, which is expressed and secreted from the SCO and the floor plate cells of the spinal cord (*7*, *31*, *38*–*40*). As described above, the transcription level of SCO-spondin has no obvious change in *dpy19l1l*$^{-/-}$ mutants compared with control sibling (fig. S6), thus raising the intriguing possibility that the RF formation is problematic in *dpy19l1l*$^{-/-}$ mutants. To test this hypothesis, we performed SCO-spondin immunostaining and wheat germ agglutinin (WGA) labeling experiments. *dpy19l1l*$^{-/-}$ mutants exhibited

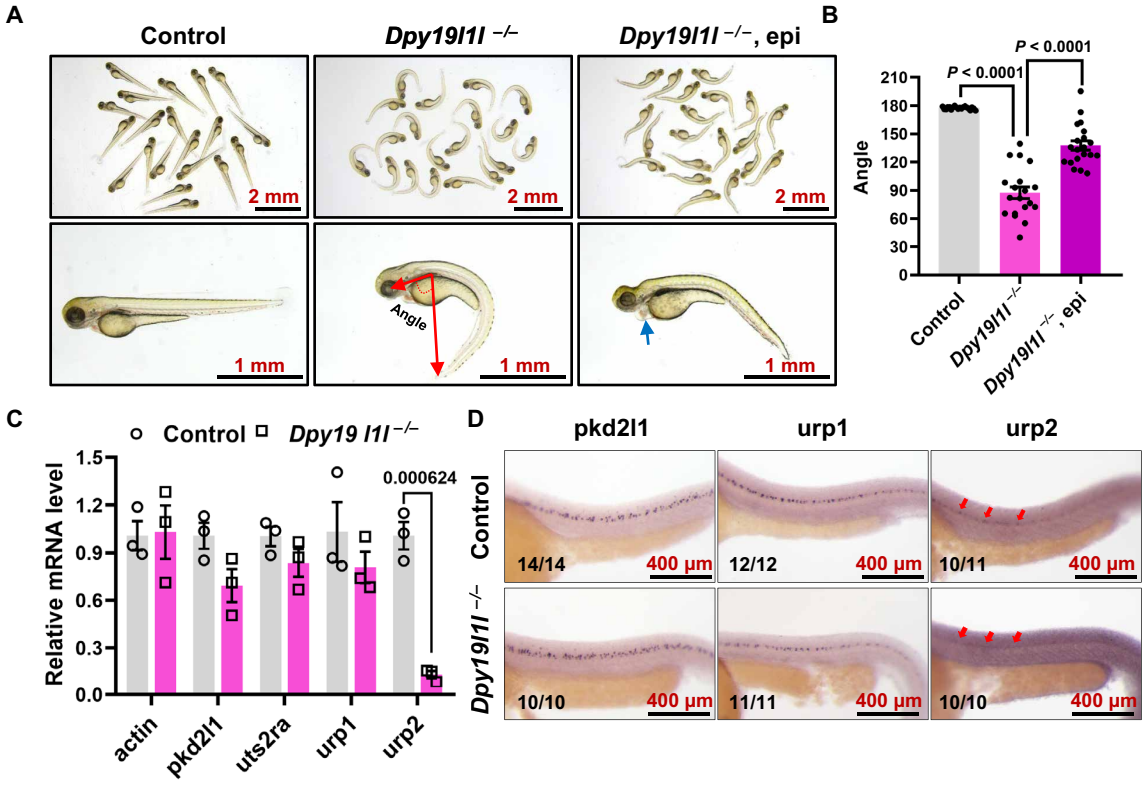

Fig. 2. *Urp2* transcription is substantial reduced in *dpy19l1l* mutants. (**A**) External phenotypes of control siblings, *dpy19l1l*$^{-/-}$ mutants, and epinephrine-treated *dpy19l1l*$^{-/-}$ mutants at 48 hpf. The schematic angle illustrates the quantification method in this study. The blue arrow indicates pericardial edema in epinephrine-treated mutants. (**B**) Body axis angles from (A) quantified with ImageJ (bar graph; means ± SEM). *P* values (unpaired *t* test) are shown above bars. (**C**) qPCR analysis of *pkd2l1*, *uts2ra*, *urp1*, and *urp2* expression in control siblings and *dpy19l1l*$^{-/-}$ mutants at 36 hpf (means ± SEM, $n = 3$; number above the bar graph represent the *P* value). (**D**) WMISH of *pkd2l1*, *urp1*, and *urp2* in control siblings and *dpy19l1l*$^{-/-}$ mutants at 36 hpf. The red arrows highlight diminished *urp2* expression.

complete absence of RF (Fig. 4A and fig. S7A). Then, our genetic rescue experiments further confirmed that this phenotype resulted specifically from *dpy19l1l* loss of function: mRNA supplementation in mutant embryos restored near-wild-type axial morphology (Fig. 4, B and C) and fully reconstituted RF structures, as evidenced by immunostaining and WGA labeling (Fig. 4D and fig. S7B). These data conclusively demonstrate that *dpy19l1l* deficiency disrupts RF formation, directly causing the observed axial curvature phenotype.

DPY19L1L mediates C-mannosylation of SCO-spondin TSRs

The overlapping expression patterns of *dpy19l1l* (Fig. 1, A and B) and *SCO-spondin* (*7*, *31*, *39*), coupled with RF absence in *dpy19l1l* mutants (Fig. 4A), raised the intriguing possibility that DPY19L1L mediates SCO-spondin to form RF through an unknown mechanism which is probably related to the C-mannosyltransferase function of DPY19L1L. Sequence analysis revealed SCO-spondin contains 20 TSR motifs (fig. S8), which are putative C-mannosylation targets of DPY19L1L (*26*, *31*, *41*, *42*). To further verify the above conjecture, we first sought to test the C-mannosylation effect of DPY19L1L on SCO-spondin by distinguishing the molecular weight of SCO-spondin in *dpy19l1l*$^{-/-}$ mutants and sibling control. However, we were unsuccessful in detecting the SCO-spondin by immunoblotting, possibly due to the high molecular weight (*39*) (5320 amino acids, >550 kDa) of SCO-spondin, which is a technical bottleneck for immunoblotting.

We therefore attempted to verify the DPY19L1L's C-mannosylation effect on SCO-spondin through a competitive inhibition strategy. On the basis of the known of C-mannosylation catalytic site of DPY-19 in *C. elegans* (*43*), we identified E106 as the homologous catalytic site of DPY19L1L (fig. S9). Also, the structure of DPY19L1L was simulated by AlphaFold (*44*, *45*). As expected, E106 locates in the core of predicted catalytic domain (Fig. 5A). Then, catalytically inactive *dpy19l1l* mRNA (E106A *mdpy19l1l*) was synthesized and injected into wild-type embryos. Nearly a third of (109/340) the E106A *mdpy19l1l*-injected embryos appeared to have body axis curved phenotype around 72 hpf (Fig. 5B and fig. S10). Then, we performed coinjection of Flag-tagged SCO-spondin TSR~20 mRNA with *dpy19l1l* or E106A *mdpy19l1l* mRNA at the ratio of 1:1 (fig. S11). The embryo lysates were collected for immunoblotting with Flag antibody. As indicated, the native Flag-TSR~20 proteins were successfully expressed in both groups. However, a trace amount of higher molecular Flag-TSR~20 was detected only in the Flag-TSR~20/*dpy19l1l* mRNA injection embryo lysate, which was deduced as the C-mannosylated Flag-TSR~20 proteins (Fig. 5C). Furthermore, SCO-spondin immunostaining result indicated that the RF was missing in E106A *mdpy19l1l* mRNA-induced body axis curvature zebrafish (Fig. 5D). Together, these results demonstrated that the role of DPY19L1L in promoting RF formation is through its C-mannosylation function to SCO-spondin TSR sequences.

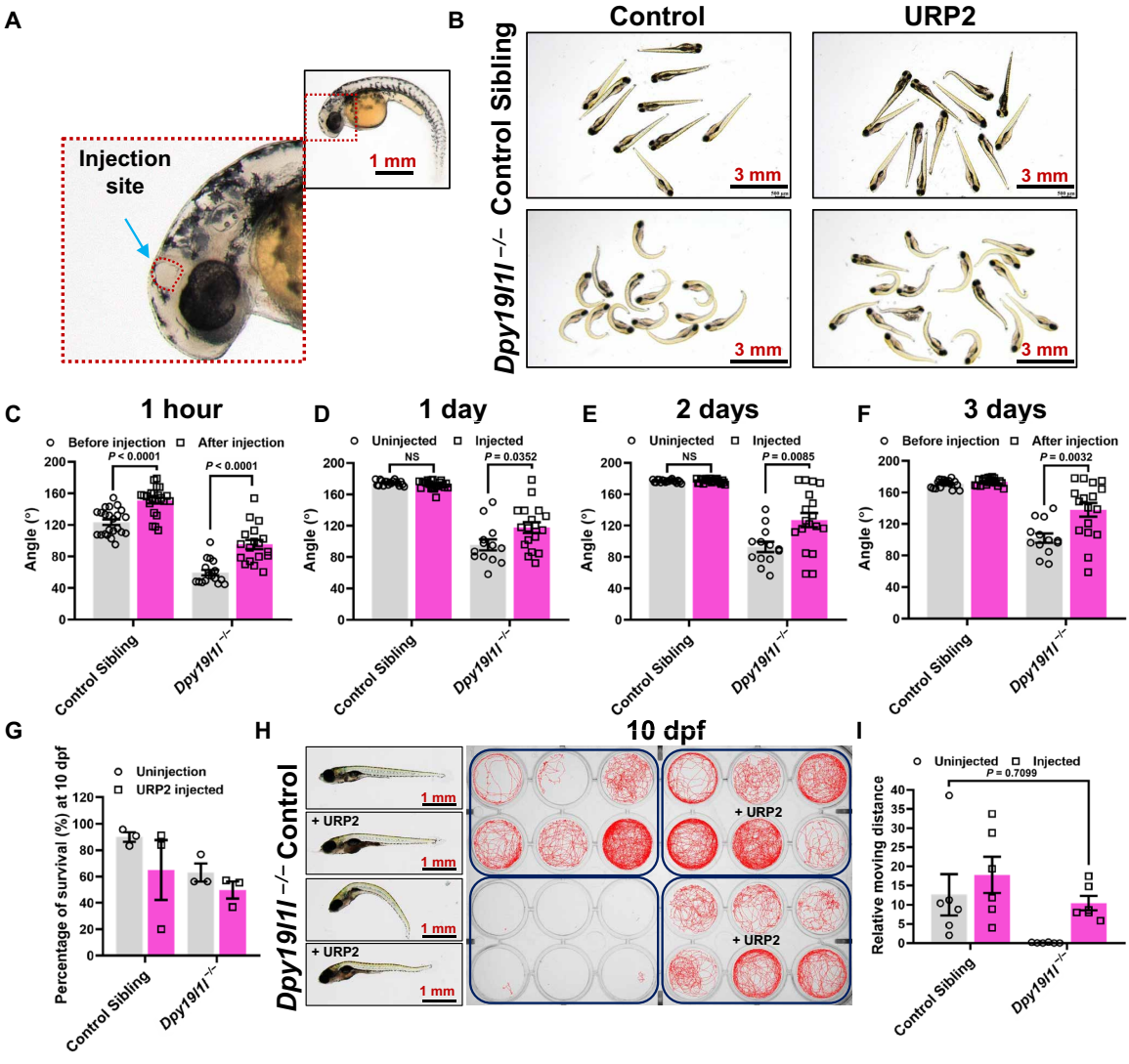

Fig. 3. URP2 injection rescues spinal curvature in *dpy19l1l*$^{-/-}$ mutants. (**A**) Schematic of URP2 injection site (cerebral ventricle marked by the blue arrow). (**B**) External phenotypes of control siblings and URP2-injected *dpy19l1l*$^{-/-}$ mutants at 3 days postinjection. (**C** to **F**) Body axis angles of URP2 injection experiment zebrafish at indicated time points, quantified with ImageJ (bar graphs; means ± SEM; *P* values above bars, unpaired *t* test). (**G**) Survival rate of URP2 injection experiment zebrafish at 10 dpf (means ± SEM). (**H**) External phenotypes (left) and swim trajectories (right) of URP2 injection experiment zebrafish at 10 dpf. (**I**) Quantification of swimming distance in (H) (means ± SEM, $n = 6$; *P* value above bar).

Most of the SCO-spondin was successfully secretion in *dpy19l1l* MO-treated zebrafish

C-mannosylation is important for folding, secretion, and interaction of the proteins containing TSR motif (*25*–*27*, *46*). To characterize whether DPY19L1L-mediated C-mannosylation of SCO-spondin affects its secretion and/or interaction (aggregation), we collected single-cell embryos of the cell membrane enhanced green fluorescent protein (EGFP)–labeled zebrafish Tg (β-actin:ras:GFP), and antisense MO oligonucleotides were injected to knock down *dpy19l1l* expression. The resulting *dpy19l1l* morphants exhibited severe body axis curvature defects, with 79% of specimens ($n = 143$) showing trunk angles below 100° (Fig. 6A). Confocal microscopy revealed that, although SCO-spondin secretion from floor plate cells into the spinal cavity was largely unaffected in *dpy19l1l* morphants compared to controls, these morphants failed to form RF (Fig. 6B). These data suggested that DPY19L1L-mediated RF formation and body axis straightening, at least in part, are through C-mannosylation of SCO-spondin TSR sequences and thus promote its' assembly in spinal cord (Fig. 7).

DISCUSSION

Is DPY19L1 functionally conserved in humans?

IS occurs in the absence of underlying vertebral anomalies, which affects 1 to 3% of children worldwide, and the mechanisms underlying this spinal deformity remain largely unknown. Clinical investigation indicates reduced methylation variability near the *dpy19l1* locus in severe IS cases compared to controls (*36*), suggesting a potential role of *dpy19l1* dysregulation in IS pathogenesis.

Although zebrafish has emerged as a powerful model for investigating the pathogenesis of IS, there is no denying that the zebrafish

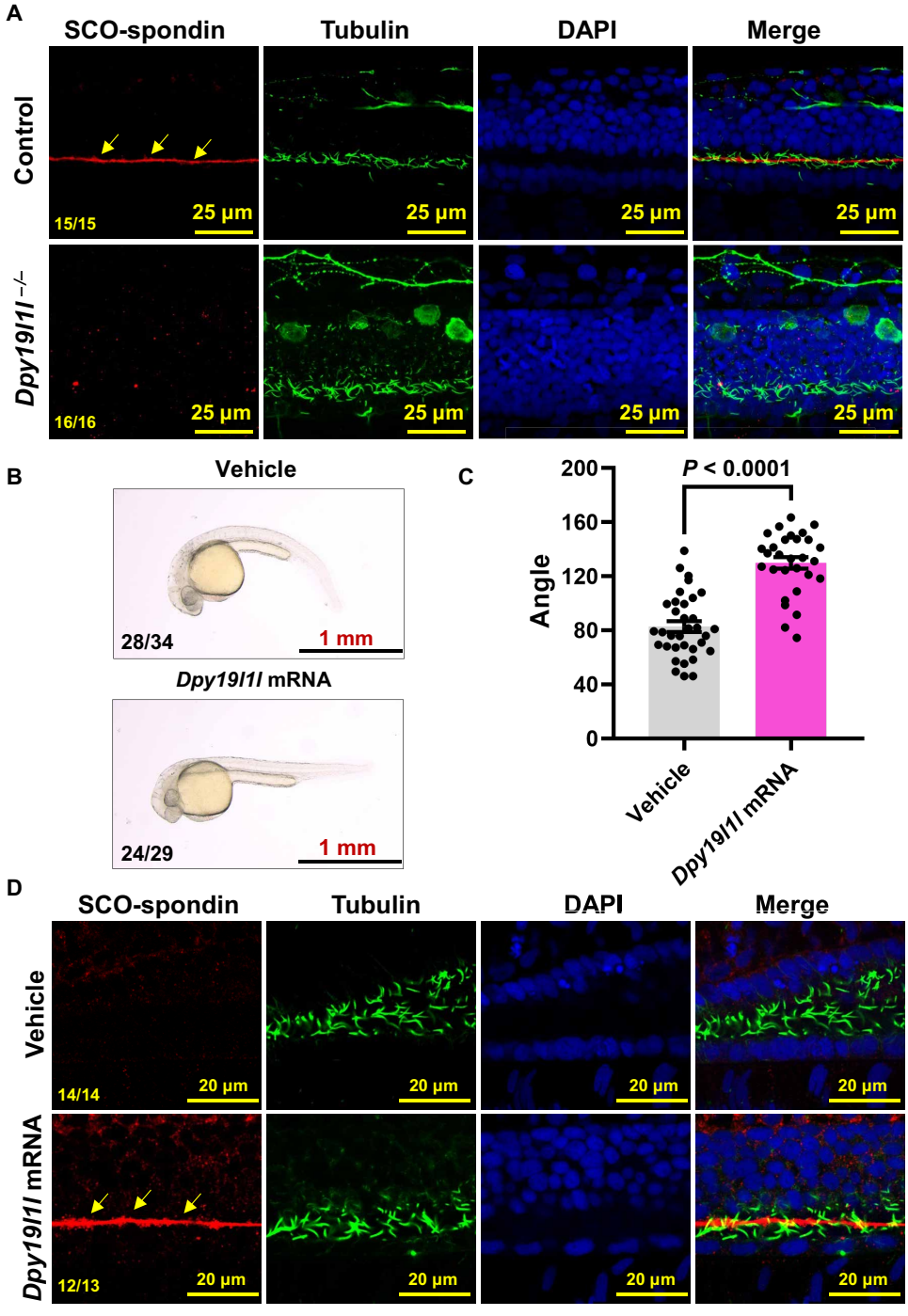

Fig. 4. *Dpy19l1l*$^{-/-}$ mutants lack RF. (**A**) Confocal images showing the location of RF by immunostaining with SCO-spondin antibody (red) and cilia antibody (green) in control siblings and *dpy19l1l*$^{-/-}$ mutants at 36 hpf. Nuclei counterstained with DAPI. Yellow arrows indicate intact RF in controls. (**B**) External phenotypes of *dpy19l1l*$^{-/-}$ mutants injected with vehicle or *dpy19l1l* mRNA at 36 hpf. (**C**) Body axis angles of mutants in (B) quantified with ImageJ (means ± SEM; *P* values above bars, unpaired *t* test). (**D**) Confocal images of the reestablished RF (red) in *dpy19l1l* mRNA-rescued mutants at 36 hpf. Yellow arrows mark reestablished RF.

is quite different from humans. For example, human SCO is well developed during fetal and neonatal stages but continues regressed during childhood (*22*, *39*, *47*). *SCO-spondin* is classified as a pseudogene in humans, and the secretion of SCO-spondin only detected at fetal stages, and RF formation have not been observed in humans, which is entirely different from zebrafish (*6*, *7*, *9*, *16*, *39*, *47*, *48*). Our study demonstrates that DPY19L1L-mediated C-mannosylation of SCO-spondin TSR motifs is essential for RF formation and axial straightening in zebrafish. This raises critical questions: Does human DPY19L1 share this conserved function, and could *dpy19l1* mutations serve as diagnostic markers for IS? Given DPY19L1L's embryonic role in zebrafish, we speculate that, if DPY19L1 has a similar

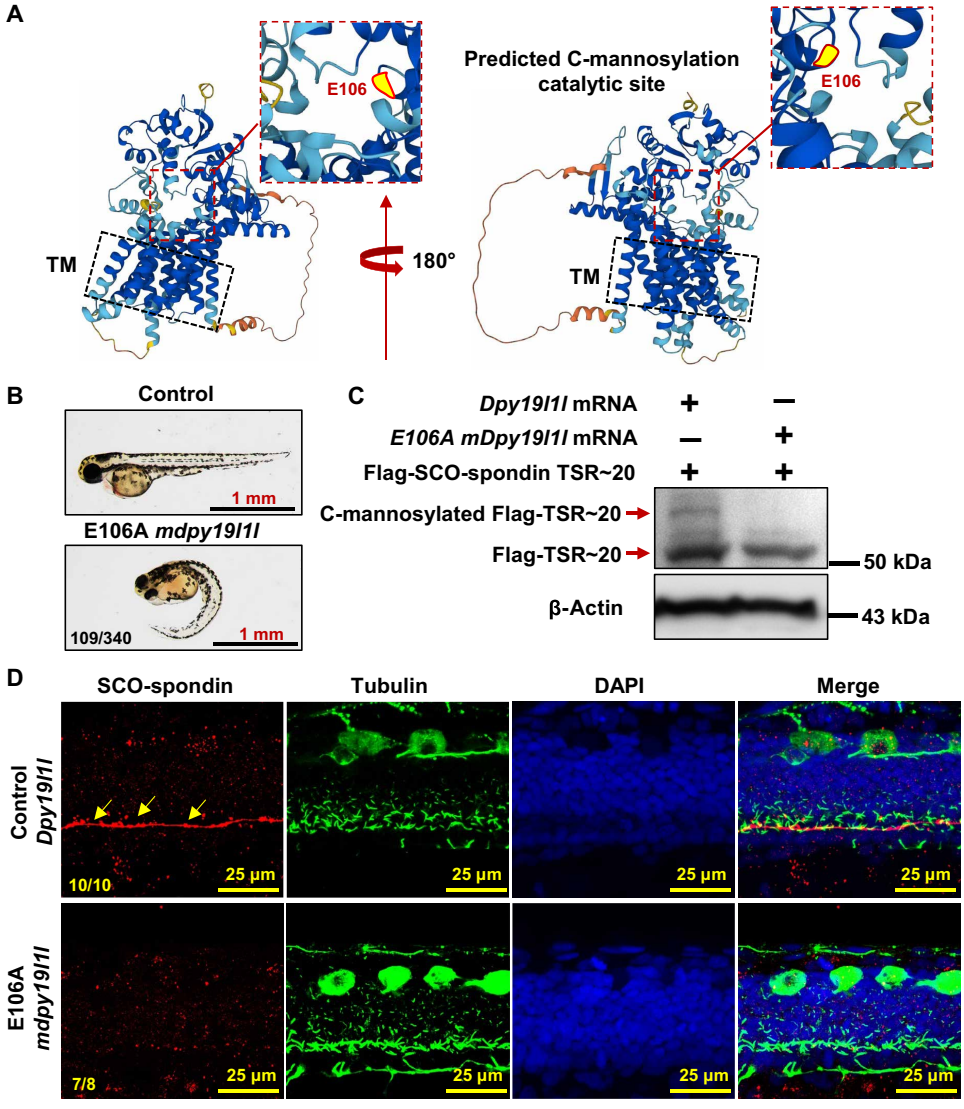

Fig. 5. DPY19L1L C-mannosylates SCO-spondin TSR motifs. (**A**) AlphaFold-predicted DPY19L1L structure. Red box highlights the catalytic core; yellow dot marks putative C-mannosylation site (E106). TM, transmembrane region. (**B**) Phenotypes of wild-type embryos injected with *E106A dpy19l1l* mRNA at 48 hpf. (**C**) Immunoblot of Flag-TSR~20 lysates from injected embryos. Anti-Flag detects Flag-TSR~20 and C-mannosylated Flag-TSR~20. (**D**) RF localization (red) in wild-type embryos injected with control or *E106A dpy19l1l* mRNA (36 hpf). Red: SCO-spondin; green: cilia; DAPI: nuclei. Yellow arrows indicate RF in controls.

function in humans, it is likely to be in fetal and neonatal stages, but this is only our speculation based on the available information, and more investigations are needed in future.

Implications for IS treatment

Current IS treatments largely rely on invasive surgeries due to limited mechanistic insights (*2*, *37*, *49*). Consistent with prior studies (*8*, *14*–*16*, *20*), we observed that URP2 alleviated spinal curvature in *dpy19l1l*$^{-/-}$ mutants (Fig. 3). Notably, *dpy19l1l*$^{-/-}$ and *SCO-spondin*$^{-/-}$ mutants (*8*) both exhibit down-regulated *urp2* (Fig. 3C), implicating URP2 as a key downstream effector of adrenergic signaling in CSF-cNs. This positions URP2 as a specific and efficient regulator of spinal alignment in zebrafish. Although URP2 shows promise in the zebrafish model, translating these findings to human IS treatment requires further investigation. The differences in the physiological and genetic backgrounds between zebrafish and humans need to be carefully considered. Future studies could focus on conducting preclinical trials to assess its safety and efficacy in mice or larger animal models more closely to humans.

RF-dependent axial morphogenesis in zebrafish

Zebrafish studies delineate a pathway wherein cilia-driven CSF flow facilitates SCO-spondin transport, RF assembly, adrenergic signaling, and urotensin-mediated axial stabilization (*1*, *6*, *7*, *9*, *14*–*16*). In this pathway, the aggregate form of SCO-spondin, i.e., the RF acts as the hub to deliver the signal molecules. Both ciliary dysfunction and *SCO-spondin* mutations cause RF deficiency and induce a similar scoliosis phenotype, which exhibits embryonic spinal downward curvature and progressing to three-dimensional (3D) spinal deformities in adults (*2*, *7*, *14*–*16*). Our *dpy19l1l*$^{-/-}$ mutants phenocopy

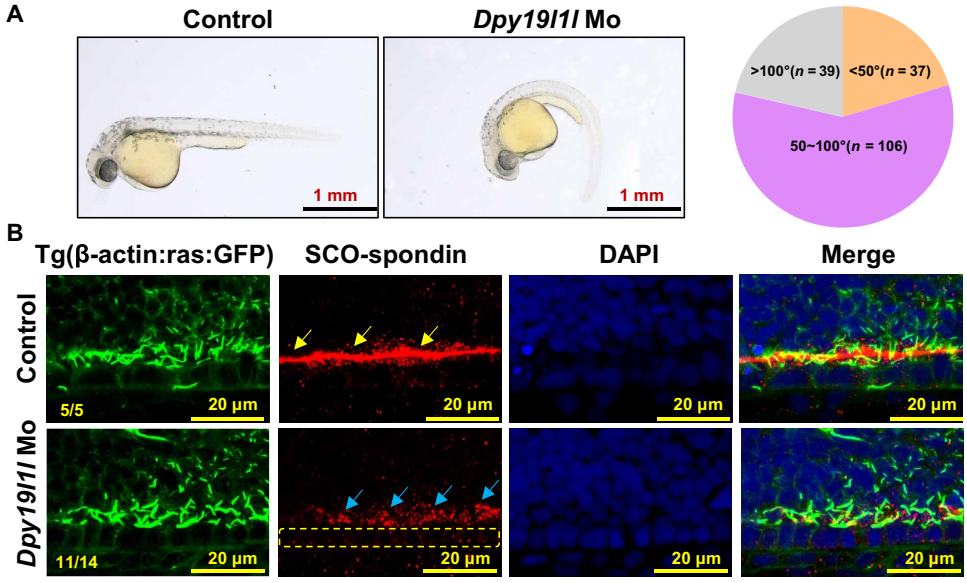

Fig. 6. SCO-spondin secretion persists in *dpy19l1l* morphants. (**A**) External phenotypes of *Tg(β-actin:ras:GFP)* embryos injected with *dpy19l1l* morpholino at 36 hpf. Pie chart: body axis angles. (**B**) RF and SCO-spondin localization in controls and *dpy19l1l* MO embryos (36 hpf). Red: SCO-spondin; green: membrane and cilia; DAPI: nuclei. Yellow arrows: intact RF; blue arrows: SCO-spondin; yellow dashed box: floor plate cells.

RF-deficient models, displaying embryonic spinal curvature and impaired RF formation.

The structure of SCO-spondin and RF are interspecies variations in different vertebrates, and the intact RF has not been found in humans (*7*, *47*, *50*). A clinical investigation found that mutation of SLC6A9 would lead to human IS, and Slc6a9 mutant zebrafish exhibited harmful neural activity and spinal curvature resembling human patients with IS (*51*). Unlike spinal downward curvature phenotype in RF defected mutants, Slc6a9 mutant zebrafish displayed an apparent lateral axial curvature and died in 18 days (*51*). SCO-spondin is a giant glycoprotein, which makes itself more susceptible to defects in expression, folding, modification, translocation, secretion, and assembly (*16*, *31*, *39*, *40*, *52*). Thus, we raise the possibility that abnormality of the genes, which are related to fulfilling intact biological function of SCO-spondin and RF in zebrafish may result in similar spinal downward curvature phenotype in larvae.

MATERIALS AND METHODS

Reagents and tools

For all antibodies, reagents, primers, software, tools, and zebrafish strains used here, refer to Table 1.

Zebrafish husbandry

All experiments were performed on zebrafish (*D. rerio*) of the AB background. Zebrafish were raised and maintained under standard laboratory conditions as previously described (*53*). All animal experiments complied with the Laboratory Animal Management Committee Cultivation guidelines and were approved by the Independent Animal Care Committee (IACC) of Gannan Normal University (approval number: GNNU2022-0628).

WMISH analysis

WMISH was performed following established protocols. Briefly, embryos were fixed overnight in 4% paraformaldehyde (PFA) at 4°C. After washing steps, embryos were dehydrated in methanol and rehydration through a graded methanol series. Then, the embryos were digested with proteinase K. Subsequent processing included methanol treatment (20 min), hybridization, blocking, and incubation with anti-Dig-AP antibody (1:2000). After washing steps, embryos were colored by coloration buffer, and reactions were terminated with stop solution. WMISH images were captured using a Leica M205FA microscope. FISH was performed according to the standard protocol provided with the TSA-plus Fluorescein System kit (PerkinElmer). Fluorescence signals in the spinal cord were captured using a Leica Sp8 confocal microscope.

ARS staining

Adult zebrafish were euthanized and fixed in 4% PFA at room temperature for 48 hours. Following fixation, the PFA solution was decanted, and embryos were sequentially dehydrated twice in 75% ethanol [prepared in phosphate-buffered saline (PBS)] for 24 hours. After ethanol removal, samples were washed three times and stained in 0.1% (w/v) ARS for 24 hours. Poststaining, zebrafish were immediately rinsed in distilled water and subjected to tissue clearing via trypsin digestion for 72 hours. The trypsin solution was then replaced with 1% KOH, with daily solution renewal over a 5-day period. Specimens were subsequently transferred to a 1% KOH-glycerol solution (3:7 v/v) for 48 hours, followed by long-term storage in 100% glycerol for skeletal analysis.

Real-time qPCR analysis

Dpy19l1l$^{+/-}$ zebrafish were intercrossed and embryos were collected. The chorion was removed at 36 hpf, followed by embryo grouping based on body axis morphology. Embryos were rinsed with RNase-free water, and total RNA was isolated using the TransZol Up Plus RNA Kit as previously described (*53*). Relative transcription levels of *SCO-spondin*, *pkd2l1*, *uts2ra*, *urp1*, and *urp2* genes were quantified using the qTOWER^{3}G RT-PCR system (Analytik Jena, Germany) based on Ct values for target genes and β-actin.

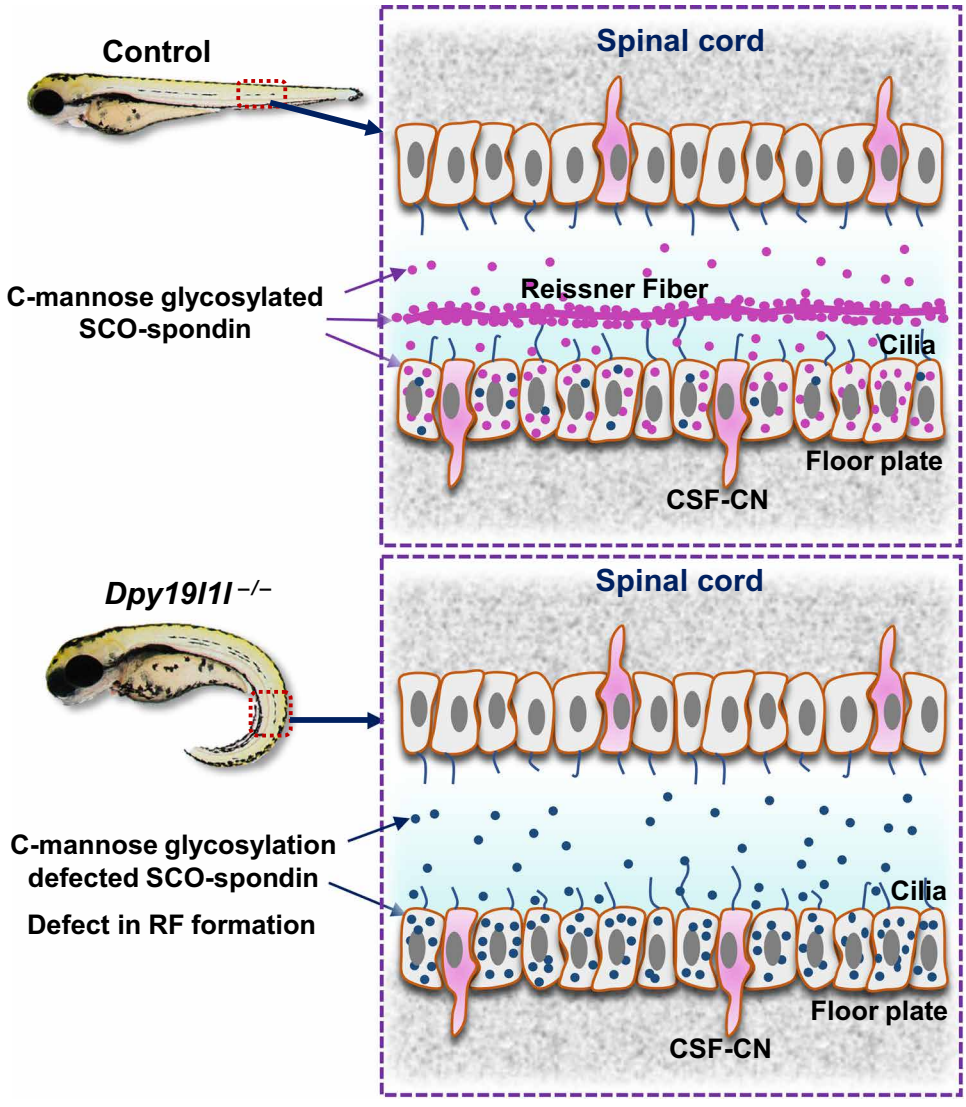

Fig. 7. Model of SCO-spondin and RF in control and *dpy19l1l*-deficient zebrafish. (**Top**) In wild-type spinal cord, DPY19L1L C-mannosylates SCO-spondin (purple), enabling RF formation via cilia-driven CSF flow. (**Bottom**) In *dpy19l1l*$^{-/-}$ mutants, nonglycosylated SCO-spondin (dark blue) fails to form RF, leading to body axis curvature. CSF-CN, CSF-contacting neuron.

Epinephrine and URP2 treatments

Control siblings and *dpy19l1*$^{-/-}$ mutants at 36 hpf were collected and grouped as described above. *Dpy19l1*$^{-/-}$ mutants were subjected to epinephrine treatment (10 mg/ml final concentration) or the same volume of vehicle for 12 hours. External phenotypes were captured using a Leica M205FA microscope, and the angles of the zebrafish were calculated. URP2 was diluted in Ringer's solution to a final concentration of 800 μg/ml as previously described (*15*), and the URP2 or vehicle was injected into the cerebral ventricle as indicated in this study. External phenotypes were captured using a Leica M205FA microscope as indicated time points in the figures, and the angles of the zebrafish were calculated.

Fluorescent tracer assay for CSF flow analysis

To quantify the CSF dynamics of control siblings and *dpy19l1l* mutants at 2 dpf, larvae were immobilized on the surface of the agarose plate, followed by injecting the FITC-Dextran fluorescent dye into the brain ventricles through a glass capillary needle as described previously (*14*, *15*). Fluorescence signals in the spinal canal were recorded every minute using a ZEISS fluorescence microscope.

Immunostaining assay

Immunostaining of whole-mount embryos using antibodies as indicated in figures were performed according the following protocol similar to that previously described (*54*). Briefly, the 36 hpf embryos were washed with PBS and fixed in 4% PFA for 2 hours at 4°C. After washing steps, incubated the embryos with blocking buffer (PBTN: PBS + 1% Triton X-100 + 4% bovine serum albumin + 0.02% NaN_3) for 2 hours at 4°C. Then, the following primary antibodies were diluted in PBTN and incubated overnight at 4°C: anti-F59 (1:100), anti-prox1a (1:100), Anti-engrailed (1:100), anti-acetylated α-tubulin (1:500), and anti-SCO-spondin (1:500). After washing with PBST

Table 1. All antibodies, reagents, primers, software, tools, and zebrafish strains used.

Reagent/resource	Reference or source	Catalog number
Antibodies		
Anti-F59	DHSB	AB_528373
Anti-prox1(prox1a)	Sigma-Aldrich	AB5475
Anti-engrailed	DHSB	AB_528224
Anti-acetylated tubulin	Sigma-Aldrich	T7451-100UL
Anti-SCO-spondin	YNK-BIOTECK	3437-1-R1/R2
Anti-Flag Tag	Proteintech	66008-4-Ig
Anti-β actin	Beyotime	AF5003
HRP-Goat Anti-Mouse IgG (H+L)	Servicebio	GB23301
Anti-Digoxigenin-AP Fab fragments	Roche	11093274910
YF 647 Goat Anti-Rabbit IgG	UE landy	Y6109L
Alexa Fluor-647 Goat Anti-mouse	Invitrogen	A21236
Alexa Fluor-488 Goat Anti-mouse	Invitrogen	A11029
Chemicals and peptides		
Epinephrine	GLPBIO	GC41670
Alizarin red	Sangon Biotech	A506786-0025
NotI-HF	NEB	R3189S
WGA	Thermo Fisher Scientific	W32464
URP2	Ocean University of China College of Marine Life Sciences, provided by C. Zhao	
FITC-Dextran	Xi'an ruixi Biological Technology Co. Ltd.	R-FD-005
Fast Mutagenesis System	TransGen Biotech	FM111-02
mMESSAGE mMACHINE SP6 Transcription kit	Ambion	AM1340
TransZol Up Plus RNA Kit	TransGen Biotech	ER501-01-V2
TSA Plus Fluorescein System	PerkinElmer Inc.	NEL741001KT
Oligonucleotides and sequence-based reagents		
CRISPR-Cas9 Guide RNA		
dpy19l1l forward	taatacgactcactataGGAATAACAGTGCTGATTCTgttttagagctagaaatagc	
SgRNA reverse	AGCACCGACTCGGTGCCACTT	
In situ hybridization primers		
dpy19l1l forward dpy19l1l reverse	ACTTCTATGTCGCTTTTGTGT TTCTCACCAATCCAGCCAAACAG	
pkd2l1 forward pkd2l1 reverse	GAATCACCTGAGCTGCGAGA taatacgactcactatagggCCGTTGATCAGTCCAAACGC	
urp1 forward urpl1 reverse	AGTCAGCCACGATCCTCTCA gactaatacgactcactatagggTTCACAATGTAAAAGGGCAGCA	
urp2 forward urp2 reverse	CGCTTCAATCGTGGATGCTG taatacgactcactatagggGGATTTGTTGCAGGCCGTTT	
SCO-spondin forward	TTTGCAGTCTGGATGGTGAAGACC	
SCO-spondin reverse	taatacgactcactatagggCGCTCCAGCTCATACAGGTGGAGG	
Morpholino oligo sequence of dpy19l1l	GGTTTTCTGGTTTTTACTACCATGT	
qPCR primers		
actin forward actin reverse	AGCACGGTATTGTGACTAACTG TCGAACATGATCTGTGTCATC	
SCO-spondin forward	ATCAAACTGTCCTCCGCTTCACT	
SCO-spondin reverse	GACAGTCGCCCTTGGTGATGTTCCT	
uts2ra forward uts2ra reverse	CTTCCCTCCCCTCATTTGCTT TCGGCCTTCATCCACACTTC	
pkd2l1 forward pkd2l1 reverse	GTGACTGTTTCGATGTGTAC CTTGATAAAACCCTGCTCCG	
urp1 forward urpl1 reverse	ACATTCTGGCTGTGGTTTG GTCCGTCTTCAACCTCTGCTAC	

(*Continued*)

(*Continued*)

Reagent/resource	Reference or source	Catalog number
urp2 forward	AGAGGAAACAGCAATGGACG	
urp2 reverse	TGTTGGTTTTCTTGGTTGACG	
Software and database		
GraphPad Prism 8	https://graphpad.com/scientific-software/prism/	
ImageJ	https://imagej.en.softonic.com/	
AlphaFold Protein Structure Database	https://alphafold.ebi.ac.uk/	
Zebrafish strains and mutants		
Wild-type AB zebrafish	National Zebrafish Resource Center (China)	
dpy19l1l−/− mutant	This manuscript	
Tg(β-actin:ras:GFP)	Provided by L. Luo	

(PBST: PBS + 1% Triton X-100), the corresponding secondary antibodies (YF 647 Goat Anti-Rabbit IgG, Alexa Fluor-647 goat anti-mouse IgG, and Alexa Fluor-488 goat anti-mouse, diluted in PBTN, 1:500) were incubated for 2 hours at room temperature in the dark. Then, the embryos were washed with PBS containing 0.1% Triton X-100 and kept in 80% glycerol lastly, and the staining signal was captured by a Leica Sp8 confocal microscope.

WGA (red) staining

WGA staining was performed as previously described (*14*). Briefly, embryos were fixed overnight at 4°C. After washing steps, the embryos were incubated with WGA staining solution (1:200) for 24 hours at 4°C. After washing steps, staining images were captured through a Leica Sp8 confocal microscope.

mRNA synthesis and treatment

The full-length coding sequence of *Dpy19l1l* was cloned into pCS2+ expression vector to generate the *pCS2-Dpy19l1l* construct. The *pCS2-E106A mDpy19l1l* mutant plasmid was engineered from the parental *pCS2-Dpy19l1l* backbone using the Fast Site-Directed Mutagenesis Kit (TransGen Biotech). Following linearization with *NotI* restriction enzyme, capped mRNA was synthesized and purified by using the mRNA transcription synthesis kits (Ambion). For rescue experiments, 150 pg of *Dpy19l1l* mRNA was microinjected into single-cell stage embryos. For the competition experiments, the *Dpy19l1l* and E106A *mDpy19l1l* mRNAs were injected at 600 pg per embryo. The chorions were dissected at 48 hpf, and the external phenotypes were captured using a Leica M205FA microscope. Then, the embryos were fixed, and standard procedures of immunofluorescence assay were carried out using anti-SCO-spondin and anti-tubulin antibodies as previously described. RF and cilia images were captured through a Leica Sp8 confocal microscope.

Immunoblotting

SCO-spondin TSR motifs nucleotides were synthesized from GenScript Biotech Corp. and cloned into the pCS2+ vector with an N-terminal FLAG epitope tag to generate pCS2-FLAG-TSR~20. Capped mRNA was synthesized as described before, and Flag-TSR~20 mRNA was mixed with *dpy19l1l* mRNA or E106A *mdpy19l1l* at the ratio of 1:1. Then, the mRNA mixtures were subjected to microinjection and the embryos were collected at 96 hpf, and the lysates were followed by immunoblotting. For immunoblotting, 50 mRNA-injected embryos at 96 hpf were collected into 200 μl of radioimmunoprecipitation assay lysis buffer, and samples followed a standard immunoblotting procedure. The dilution ratio of Anti-Flag tag antibody was 1:1000, and Goat Anti-Mouse IgG was 1:5000. Blots exposure signals were collected by an Analytik Jena UVP ChemStudio imaging system.

MO microinjection

Wild-type or *Tg(β-actin:ras:GFP)* zebrafish embryos were collected for microinjection. MO was diluted by ddH_2O with a final concentration of 500 μM, and 1 nl of the MO was injected into the animal pole of the embryos. The chorions were dissected at 36 hpf, and the external phenotypes were captured and analyzed as described above. The *Tg(β-actin:ras:GFP)* zebrafish were fixed, and standard procedures of immunofluorescence assay were carried out using SCO-spondin antibody as described above. RF, cilia, and floor plate cell membrane images were captured through a Leica Sp8 confocal microscope.

Statistical analysis

All of the angle measurements in this study were performed through ImageJ software. All bar graphs were presented as means ± SEM, and the dots indicated individual values. The *P* values were determined using the multiple *t* tests function in GraphPad Prism 8 (two-stage linear step-up procedure of Benjamini, Krieger, and Yekutieli with *Q* set to 5%). A value of $P < 0.05$ was considered statistically significant, and $P > 0.05$ was considered statistically not significant (NS). All experiments in this study were replicated successfully.

Supplementary Materials

This PDF file includes:

Figs. S1 to S11

REFERENCES AND NOTES

1. C. W. Boswell, B. Ciruna, Understanding idiopathic scoliosis: A new zebrafish school of thought. *Trends Genet.* **33**, 183–196 (2017).

2. D. T. Grimes, C. W. Boswell, N. F. C. Morante, R. M. Henkelman, R. D. Burdine, B. Ciruna, Zebrafish models of idiopathic scoliosis link cerebrospinal fluid flow defects to spine curvature. *Science* **352**, 1341–1344 (2016).
3. Z. Su, Y. Yang, S. Wang, S. Zhao, H. Zhao, X. Li, Y. Niu, Deciphering Disorders Involving Scoliosis and COmorbidities (DISCO) Study Group, G. Qiu, Z. Wu, N. Wu, T. J. Zhang, The mutational landscape of *PTK7* in congenital scoliosis and adolescent idiopathic scoliosis. *Genes* **12**, 1791 (2021).
4. M. Hayes, X. Gao, L. X. Yu, N. Paria, R. M. Henkelman, C. A. Wise, B. Ciruna, *ptk7* mutant zebrafish models of congenital and idiopathic scoliosis implicate dysregulated Wnt signalling in disease. *Nat. Commun.* **5**, 4777 (2014).
5. Z. Liu, Y. Hai, Z. Li, L. Wu, Zebrafish and idiopathic scoliosis: The 'unknown knowns'. *Trends Genet.* **38**, 524–528 (2022).
6. Y. Cantaut-Belarif, J. R. Sternberg, O. Thouvenin, C. Wyart, P.-L. Bardet, The Reissner fiber in the cerebrospinal fluid controls morphogenesis of the body axis. *Curr. Biol.* **28**, 2479–2486.e4 (2018).
7. B. R. Troutwine, P. Gontarz, M. J. Konjikusic, R. Minowa, A. Monstad-Rios, D. S. Sepich, R. Y. Kwon, L. Solnica-Krezel, R. S. Gray, The Reissner fiber is highly dynamic in vivo and controls morphogenesis of the spine. *Curr. Biol.* **30**, 2353–2362.e3 (2020).
8. Y. Cantaut-Belarif, A. O. Del'Immagine, M. Penru, G. Pézeron, C. Wyart, P.-L. Bardet, Adrenergic activation modulates the signal from the Reissner fiber to cerebrospinal fluid-contacting neurons during development. *Elife* **9**, e59469 (2020).
9. W. Driever, Developmental biology: Reissner's fiber and straightening of the body axis. *Curr. Biol.* **28**, R833–R835 (2018).
10. C. Muñoz-Montecinos, A. Romero, V. Sepúlveda, M. Á. Vira, K. Fehrmann-Cartes, S. Marcellini, F. Aguilera, T. Caprile, R. Fuentes, Turning the curve into straight: Phenogenetics of the spine morphology and coordinate maintenance in the zebrafish. *Front. Cell Dev. Biol.* **9**, 801652 (2022).
11. C. D. Rose, D. Pompili, K. Henke, J. L. M. Van Gennip, A. Meyer-Miner, R. Rana, S. Gobron, M. P. Harris, M. Nitz, B. Ciruna, SCO-spondin defects and neuroinflammation are conserved mechanisms driving spinal deformity across genetic models of idiopathic scoliosis. *Curr. Biol.* **30**, 2363–2373.e6 (2020).
12. A. Orts-Del'Immagine, Y. Cantaut-Belarif, O. Thouvenin, J. Roussel, A. Baskaran, D. Langui, F. Koëth, P. Bivas, F.-X. Lejeune, P.-L. Bardet, C. Wyart, Sensory neurons contacting the cerebrospinal fluid require the Reissner fiber to detect spinal curvature in vivo. *Curr. Biol.* **30**, 827–839.e4 (2020).
13. C. Ringers, N. Jurisch-Yaksi, Development: How the Reissner fiber keeps our back straight. *Curr. Biol.* **30**, R705–R708 (2020).
14. H. Xie, Y. Kang, J. Liu, M. Huang, Z. Dai, J. Shi, S. Wang, L. Li, Y. Li, P. Zheng, Y. Sun, Q. Han, J. Zhang, Z. Zhu, L. Xu, P. C. Yelick, M. Cao, C. Zhao, Ependymal polarity defects coupled with disorganized ciliary beating drive abnormal cerebrospinal fluid flow and spine curvature in zebrafish. *PLOS Biol.* **21**, e3002008 (2023).
15. X. Zhang, S. Jia, Z. Chen, Y. L. Chong, H. Xie, D. Feng, X. Wu, D. Z. Song, S. Roy, C. Zhao, Cilia-driven cerebrospinal fluid flow directs expression of urotensin neuropeptides to straighten the vertebrate body axis. *Nat. Genet.* **50**, 1666–1673 (2018).
16. H. Lu, A. Shagirova, J. L. Goggi, H. L. Yeo, S. Roy, Reissner fibre-induced urotensin signalling from cerebrospinal fluid-contacting neurons prevents scoliosis of the vertebrate spine. *Biol. Open* **9**, bio052027 (2020).
17. J. L. M. Van Gennip, C. W. Boswell, B. Ciruna, Neuroinflammatory signals drive spinal curve formation in zebrafish models of idiopathic scoliosis. *Sci. Adv.* **4**, eaav1781 (2018).
18. T. Caprile, S. Hein, S. Rodriguez, H. Montecinos, E. Rodriguez, Reissner fiber binds and transports away monoamines present in the cerebrospinal fluid. *Mol. Brain Res.* **110**, 177–192 (2003).
19. M. Bagnat, R. S. Gray, Development of a straight vertebrate body axis. *Development* **147**, dev175794 (2020).
20. E. A. Bearce, D. T. Grimes, On being the right shape: Roles for motile cilia and cerebrospinal fluid flow in body and spine morphology. *Semin. Cell Dev. Biol.* **110**, 104–112 (2021).
21. S. Rodriguez, T. Caprile, Functional aspects of the subcommissural organ-Reissner's fiber complex with emphasis in the clearance of brain monoamines. *Microsc. Res. Tech.* **52**, 564–572 (2001).
22. H. Inada, L. G. Corales, N. Osumi, A novel feature of the ancient organ: A possible involvement of the subcommissural organ in neurogenic/gliogenic potential in the adult brain. *Front. Neurosci.* **17**, 1141913 (2023).
23. J. Hofsteenge, D. R. Muller, T. de Beer, A. Loffler, W. J. Richter, J. F. G. Vliegenthart, New type of linkage between a carbohydrate and a protein: C-glycosylation of a specific tryptophan residue in human RNase Us. *Biochemistry* **33**, 13524–13530 (1994).
24. R. G. Spiro, Protein glycosylation: Nature, distribution, enzymatic formation, and disease implications of glycopeptide bonds. *Glycobiology* **12**, 43R–56R (2002).
25. A. Shcherbakova, M. Preller, M. H. Taft, J. Pujols, S. Ventura, B. Tiemann, F. F. R. Buettner, H. Bakker, C-mannosylation supports folding and enhances stability of thrombospondin repeats. *Elife* **8**, e52978 (2019).
26. A. Shcherbakova, B. Tiemann, F. F. R. Buettner, H. Bakker, Distinct *C*-mannosylation of netrin receptor thrombospondin type 1 repeats by mammalian DPY19L1 and DPY19L3. *Proc. Natl. Acad. Sci. U.S.A.* **114**, 2574–2579 (2017).
27. S. Lopaticki, R. McConville, A. John, N. Geoghegan, S. D. Mohamed, L. Verzier, R. W. J. Steel, C. Evelyn, M. T. O'Neill, N. M. Soler, N. E. Scott, K. L. Rogers, E. D. Goddard-Borger, J. A. Boddey, Tryptophan C-mannosylation is critical for *Plasmodium falciparum* transmission. *Nat. Commun.* **13**, 4400 (2022).
28. J. Hofsteenge, M. Blommers, D. Hess, A. Furmanek, O. Miroshnichenko, The four terminal components of the complement system AreC-mannosylated on multiple tryptophan residues. *J. Biol. Chem.* **274**, 32786–32794 (1999).
29. J. C. Adams, R. P. Tucker, The thrombospondin type 1 repeat (TSR) superfamily: Diverse proteins with related roles in neuronal development. *Dev. Dyn.* **218**, 280–299 (2000).
30. A. Furmanek, J. Hofsteenge, Protein C-mannosylation: Facts and questions. *Acta Biochim. Pol.* **47**, 781–789 (2000).
31. O. Meiniel, R. Meiniel, F. Lalloué, R. Didier, M.-O. Jauberteau, A. Meiniel, D. Petit, The lengthening of a giant protein: When, how, and why? *J. Mol. Evol.* **66**, 1–10 (2008).
32. K. Watanabe, N. Bizen, N. Sato, H. Takebayashi, Endoplasmic reticulum-localized transmembrane protein Dpy19L1 is required for neurite outgrowth. *PLOS ONE* **11**, e0167985 (2016).
33. Y. Niwa, T. Suzuki, N. Dohmae, S. Simizu, Identification of DPY19L3 as the *C*-mannosyltransferase of R-spondin1 in human cells. *Mol. Biol. Cell* **27**, 744–756 (2016).
34. F. F. R. Buettner, A. Ashikov, B. Tiemann, L. Lehle, H. Bakker, *C. elegans* DPY-19 Is a *C*-mannosyltransferase glycosylating thrombospondin repeats. *Mol. Cell* **50**, 295–302 (2013).
35. K. Watanabe, H. Takebayashi, A. K. Bepari, S. Esumi, Y. Yanagawa, N. Tamamaki, Dpy19l1, a multi-transmembrane protein, regulates the radial migration of glutamatergic neurons in the developing cerebral cortex. *Development* **139**, 1225 (2012).
36. P. Carry, E. Terhune, G. Trahan, L. Vanderlinden, C. Wethey, P. Ebrahimi, F. McGuigan, K. Åkesson, N. Hadley-Miller, Severity of idiopathic scoliosis is associated with differential methylation: An epigenome-wide association study of monozygotic twins with idiopathic scoliosis. *Genes* **12**, 1191 (2021).
37. D. T. Grimes, Developmental biology: Go with the flow to keep the body straight. *Curr. Biol.* **29**, R101–R103 (2019).
38. R. I. Muñoz, T. Kähne, H. Herrera, S. Rodríguez, M. M. Guerra, K. Vío, R. Hennig, E. Rapp, E. Rodríguez, The subcommissural organ and the Reissner fiber: Old friends revisited. *Cell Tissue Res.* **375**, 507–529 (2019).
39. V. Sepúlveda, F. Maurelia, M. González, J. Aguayo, T. Caprile, SCO-spondin, a giant matricellular protein that regulates cerebrospinal fluid activity. *Fluids Barriers CNS* **18**, 45 (2021).
40. E. M. Rodríguez, S. Rodríguez, S. Hein, The subcommissural organ. *Microsc. Res. Tech.* **41**, 98–123 (1998).
41. S. Gobron, I. Creveaux, R. Meiniel, R. Didier, A. Herbet, M. Bamdad, F. El Bitar, B. Dastugue, A. Meiniel, Subcommissural organ/Reissner's fiber complex: Characterization of SCO-spondin, a glycoprotein with potent activity on neurite outgrowth. *Glia* **32**, 177–191 (2000).
42. A. Meiniel, R. Meiniel, N. Gonçalves-Mendes, I. Creveaux, R. Didier, B. Dastugue, The thrombospondin type 1 repeat (TSR) and neuronal differentiation: Roles of SCO-spondin oligopeptides on neuronal cell types and cell lines. *Int. Rev. Cytol.* **230**, 1–39 (2003).
43. J. S. Bloch, A. John, R. Mao, S. Mukherjee, J. Boilevin, R. N. Irobalieva, T. Darbre, N. E. Scott, J.-L. Reymond, A. A. Kossiakoff, E. D. Goddard-Borger, K. P. Locher, Structure, sequon recognition and mechanism of tryptophan *C*-mannosyltransferase. *Nat. Chem. Biol.* **19**, 575–584 (2023).
44. J. Jumper, R. Evans, A. Pritzel, T. Green, M. Figurnov, O. Ronneberger, K. Tunyasuvunakool, R. Bates, A. Žídek, A. Potapenko, A. Bridgland, C. Meyer, S. A. A. Kohl, A. J. Ballard, A. Cowie, B. Romera-Paredes, S. Nikolov, R. Jain, J. Adler, T. Back, S. Petersen, D. Reiman, E. Clancy, M. Zielinski, M. Steinegger, M. Pacholska, T. Berghammer, S. Bodenstein, D. Silver, O. Vinyals, A. W. Senior, K. Kavukcuoglu, P. Kohli, D. Hassabis, Highly accurate protein structure prediction with AlphaFold. *Nature* **596**, 583–589 (2021).
45. M. Varadi, S. Anyango, M. Deshpande, S. Nair, C. Natassia, G. Yordanova, D. Yuan, O. Stroe, G. Wood, A. Laydon, A. Žídek, T. Green, K. Tunyasuvunakool, S. Petersen, J. Jumper, E. Clancy, R. Green, A. Vora, M. Lutfi, M. Figurnov, A. Cowie, N. Hobbs, P. Kohli, G. Kleywegt, E. Birney, D. Hassabis, S. Velankar, AlphaFold Protein Structure Database: Massively expanding the structural coverage of protein-sequence space with high-accuracy models. *Nucleic Acids Res.* **50**, D439–D444 (2022).
46. M. Frank, D. Beccati, B. R. Leeflang, J. F. G. Vliegenthart, C-Mannosylation enhances the structural stability of human RNase 2. *iScience* **23**, 101371 (2020).
47. E. M. Rodriguez, A. Oksche, H. Montecinos, Human subcommissural organ, with particular emphasis on its secretory activity during the fetal life. *Microsc. Res. Tech.* **52**, 573–590 (2001).
48. E. Ortega, R. I. Muñoz, N. Luza, F. Guerra, M. Guerra, K. Vio, R. Henzi, J. Jaque, S. Rodriguez, J. P. McAllister, E. Rodriguez, The value of early and comprehensive diagnoses in a human fetus with hydrocephalus and progressive obliteration of the aqueduct of Sylvius: Case Report. *BMC Neurol.* **16**, 45 (2016).
49. J. C. Cheng, R. M. Castelein, W. C. Chu, A. J. Danielsson, M. B. Dobbs, T. B. Grivas, C. A. Gurnett, K. D. Luk, A. Moreau, P. O. Newton, I. A. Stokes, S. L. Weinstein, R. G. Burwell, Adolescent idiopathic scoliosis. *Nat. Rev. Dis. Primers.* **1**, 15030 (2015).

50. H. Xu, G. P. Dugué, Y. Cantaut-Belarif, F.-X. Lejeune, S. Gupta, C. Wyart, M. K. Lehtinen, SCO-spondin knockout mice exhibit small brain ventricles and mild spine deformation. *Fluids Barriers CNS* **20**, 89 (2023).
51. X. Wang, M. Yue, J. P. Y. Cheung, P. W. H. Cheung, Y. Fan, M. Wu, X. Wang, S. Zhao, A. M. Khanshour, J. J. Rios, Z. Chen, X. Wang, W. Tu, D. Chan, Q. Yuan, D. Qin, G. Qiu, Z. Wu, T. J. Zhang, S. Ikegawa, N. Wu, C. A. Wise, Y. Hu, K. D. K. Luk, Y.-Q. Song, B. Gao, Impaired glycine neurotransmission causes adolescent idiopathic scoliosis. *J. Clin. Invest.* **134**, e168783 (2024).
52. S. Gobron, H. Monnerie, R. Meiniel, I. Creveaux, W. Lehmann, D. Lamalle, B. Dastugue, A. Meiniel, SCO-spondin: A new member of the thrombospondin family secreted by the subcommissural organ is a candidate in the modulation of neuronal aggregation. *J. Cell Sci.* **109**, 1053–1061 (1996).
53. L. Huang, K. Jia, H. Xiong, G. Tian, J. Xu, W. Yuan, C. Lu, X. Xiao, H. Lu, Oxyfluorfen exposure can cause acute kidney injury by promoting ROS-induced oxidative stress and inflammation in zebrafish. *J. Hazard. Mater.* **440**, 129823 (2022).
54. J. R. Sternberg, A. E. Prendergast, L. Brosse, Y. Cantaut-Belarif, O. Thouvenin, A. Orts-Del'Immagine, L. Castillo, L. Djenoune, S. Kurisu, J. R. McDearmid, P.-L. Bardet, C. Boccara, H. Okamoto, P. Delmas, C. Wyart, Pkd2l1 is required for mechanoception in cerebrospinal fluid-contacting neurons and maintenance of spine curvature. *Nat. Commun.* **9**, 3804 (2018).

Acknowledgments: We wish to thank C. Zhao and H. Xie for support of URP2 peptides, WAG staining method, and plasmids. We thank L. Luo for kindly providing technical guidance and the *Tg(β-actin:ras:GFP)* zebrafish. We thank X. Liu, H. Xiao, Z. Wu, and J. Xu for great help in this research. **Funding:** This work was supported by the National Key R&D Program of China [2018YFA0801000 (H.L.)], National Natural Science Foundation of China [31771606 and 32170853 (H.L.), and 32460181 (G.T.)], the Natural Science Foundation of Jiangxi Province [20212ACB205007(H.L.), 20242BAB25152 and 20224BAB213034 (G.T.), and 20212BAB215001 (W.Y.)], and the Science and Technology Foundation of the Education Department of Jiangxi Province [GJJ211449 (G.T.), GJJ201002 (H.L.), and GJJ201441 (B.C.)]. **Author contributions:** Conceptualization: H.L., G.T., L.H., and Z.X. Methodology: G.T., H.L., L.H., Q.L., Y.W., J.G., and Z.X. Software: Q.L. Validation: C.L., L.H., J.G., Q.L., H.L., Z.L., B.C., Z.X., G.T., and Y.W. Formal analyses: C.L., L.H., H.L., Z.L., B.C., Z.X., and G.T. Resources: H.L., G.T., Q.L., B.C., and X.L. Investigation: G.T., H.L., L.H., Z.X., C.L., X.L., J.G., Z.L., and Y.W. Data curation: G.T., Z.X., and Z.L. Visualization: G.T., H.L., and Z.X. Writing—original draft: G.T. Writing—review and editing: H.L., G.T., Z.X., L.H., J.G., Q.L., Z.L., and B.C. Funding acquisition: H.L., G.T., Y.W., and B.C. Supervision: H.L., G.T., and X.L. Project administration: H.L. and G.T. **Competing interests:** The authors declare that they have no conflict of interest. **Data and materials availability:** All data needed to evaluate the conclusions in the paper are present in the paper and the Supplementary Materials.

Submitted 9 December 2024
Accepted 4 April 2025
Published 9 May 2025
10.1126/sciadv.adv2032